Proceedings of Global Power and Propulsion Society
ISSN-Nr: 2504-4400
GPPS Chania22
18th–20th September, 2022

www.gpps.global

GPPS-TC-2022-0070

ASSESSMENT OF TABULATED CHEMISTRY MODELS FOR THE LES OF A MODEL AERO-ENGINE COMBUSTOR

Ambrus Both
Barcelona Supercomputing Center (BSC)
ambrus.both@bsc.es
Barcelona, Spain

Daniel Mira
Barcelona Supercomputing Center (BSC)
daniel.mira@bsc.es
Barcelona, Spain

Oriol Lehmkuhl
Barcelona Supercomputing Center (BSC)
oriol.lehmkuhl@bsc.es
Barcelona, Spain

ABSTRACT

Tabulated chemistry methods present a compromise between computational cost and the ability to capture complex combustion physics in high-fidelity numerical simulations. The application of such models entails a number of modeling decisions, that may affect the simulation results significantly, especially in partially premixed combustion, where the assumption of the existence of underlying premixed or non-premixed flamelet structures is arguable. In this work, different classical tabulation strategies are assessed in terms of their ability to predict the lift-off induced by localized extinction in a model aero-engine combustion chamber: the Cambridge swirl spray flame. The lift-off dynamics of the stable n-heptane spray flame are compared using: i) premixed flamelets, ii) stable and unstable counterflow diffusion flamelets, iii) stable and unsteady extinguishing counterflow diffusion flamelets, iv) unsteady extinguishing and reigniting counterflow diffusion flamelets at a given strain rate. The extinction and reignition events associated to the lift-off are validated against OH-PLIF measurements, and the temporal evolution of the lift-off and reattachment is analyzed.

INTRODUCTION

The usage of liquid fuels prevails in the aerospace industry motivated by their high energy density and the maturity of the technology. Nevertheless, the continuous development of the existing solutions and the discovery of new disruptive combustion technologies require more and more insight into the details of the underlying physical processes and their effect on the macroscopic behavior of the propulsion system. Numerical simulations became an integral part of this development process, with ever-increasing resources dedicated to large eddy simulation (LES) (Pitsch, 2006). LES captures the transient nature of combustion, and thus it provides valuable information on the operating limits of combustors and pollutant formation. In particular, this study focuses on LES coupled with tabulated chemistry methods. A comprehensive review of frequently used methods is presented by Fiorina et al. (2015).

This study is focused on the LES of a model aero-engine combustion chamber: the Cambridge swirl spray flame. (Sidey et al., 2017) The configuration is illustrated on Fig. 1a. Air is introduced to the burner through an annular duct of outer diameter of 37 mm. Guide vanes are placed in the air inlet at an angle of 60°, inducing swirling flow of geometric swirl number: $S = 1.23$. (Cavaliere et al., 2013) Downstream the swirler, the annular duct is narrowed in two sudden steps to a final width of 6 mm where it reaches the combustion chamber. The central part of this annular duct is a bluff body of final diameter: $D_b = 25$ mm, that, together with the effect of the swirl, creates a strong central recirculation zone (CRZ) stabilizing the flame. Liquid fuel is introduced in the center of the bluff body by a pressure swirl atomizer, creating a hollow-cone spray pattern of nominal spray angle: 60°. The swirling air flow and the spray enters the rectangular combustion chamber of cross section: 95 mm × 95 mm and length: 150 mm. The flame consists of an inner reaction zone located within the hollow spray cone, and an outer reaction zone located in the shear layer that forms at the perimeter of the bluff body. Latter shows high intermittency due to strain induced local extinction. The outlet of the combustion chamber is open to the atmosphere, and the system is operated without preheating any of the reactants.

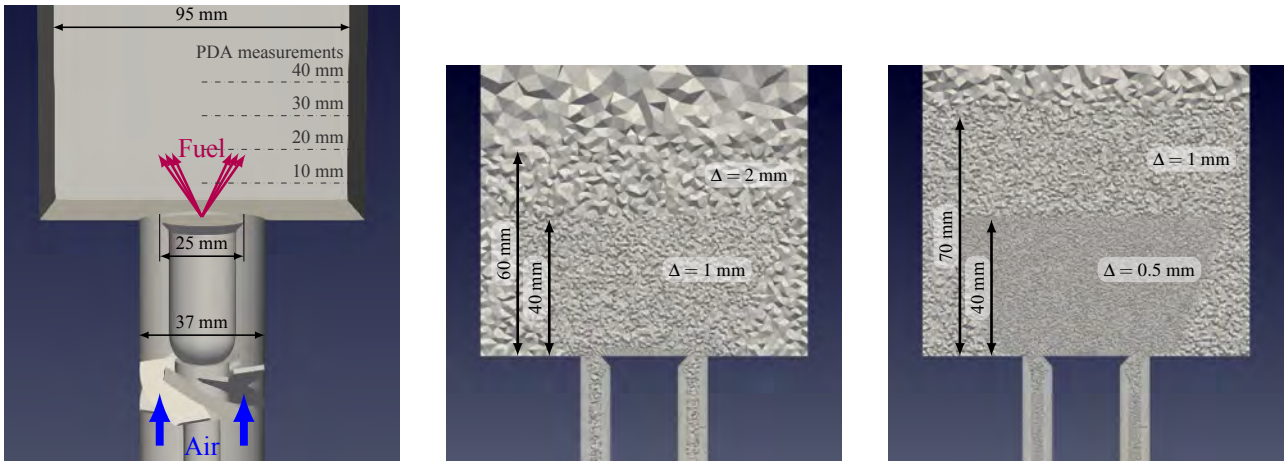

(a) Burner geometry with dimensions and the PDA measurement locations.

(b) Coarse mesh of 4M elements and 1.2M nodes.

(c) Fine mesh of 17.2M elements and 3.4M nodes.

Figure 1 Illustration of the Cambridge swirl spray flame burner geometry and computational meshes.

The Cambridge swirl flames have been the subject of various LES studies. Giusti and Mastorakos (2017) studied the stable ethanol flame of this configuration using Conditional Moment Closure (CMC) analyzing strain induced localized extinction. Paulhiac et al. (2020) studied the flame structure of an n-heptane flame using a 2-step chemistry mechanism, although under significantly different conditions ($\dot{m}_f = 0.12$ g/s, $U_b = 14.8$ m/s). Elasrag and Li (2018) used a tabulated chemistry approach based on counterflow diffusion flamelets to simulate the stable n-heptane flames. Foale et al. (2021) used CMC to investigate the global extinction of kerosene flame of this database. Finally, the authors of the present study also simulated the stable n-heptane and n-dodecane flames of this configuration using tabulated chemistry based on counterflow diffusion flamelets. (Both et al., 2021*a*)

Paulhiac et al. (2020) identified the prevalence of a non-premixed flame structure, however, they also present a significantly richer mixture fraction field ($\max(Z) = 0.35$) than that of the present simulations ($\max(Z) = 0.25$) reported in (Both et al., 2021*a*). The existing LES studies based on CMC and tabulated chemistry models all assume, that the flame structure is best represented by the counterflow diffusion flamelet configuration. However, spray flames are partially-premixed, making the selection of premixed or diffusion flamelet structure open to question.

To settle this argument Franzelli et al. (2013) and Olguin and Gutheil (2014) studied a counterflow configuration, with one of the streams corresponding to pure oxidizer and the other to a carrier oxidizer stream carrying a mono-disperse spray cloud. They found a unique behavior associated to the presence of evaporative source terms, that is not addressed by the classical tabulation methods. Nevertheless, as Franzelli et al. (2017) showed *a posteriori*, a tabulation method based on free premixed flamelets may provide adequate results in terms of flame propagation. They demonstrated the adequacy of the method on a model gas turbine combustor, that exhibits lean to stoichiometric mixture fractions throughout the domain. More recently Sacomano Filho et al. (2018) revisited the issue of laminar spray flame propagation in a plug-flow configuration, that decouples the strain effects from the evaporation. Their results confirm, that in such a configuration the application of free and burner stabilized premixed flamelets is justified, at least in terms of propagation speed.

As Paulhiac et al. (2020) shows, the Cambridge swirl spray flames exhibit various regions with drastically different characteristics, and the droplet-flame interactions studied by Franzelli et al. (2017) and Olguin and Gutheil (2014) are more important in some regions than others. In particular, the the outer reaction zone does not interact with the spray at all. The localized extinction of this reaction layer creates edge flames (triple flames) that propagate along the shear layer. As Illana et al. (2021) shows, the prediction of such flame structures is challenging for the classical tabulated chemistry methods if the mixture fraction profiles range from very low to very high values. Nevertheless, Van Oijen and De Goey (2004) achieved good prediction using premixed flamelets if the mixture fraction is within the flammability limit. In the present study, the n-heptane case (H1S1) of the Cambridge swirl flames data repository is simulated with LES using different tabulated chemistry approaches to assess this hypothesis, by comparing four different tabulation methods.

The H1S1 case is characterized by a fuel mass flow rate of $\dot{m}_f = 0.27$ g/s and a bulk air velocity of $U_b = 17.11$ m/s evaluated at the inlet of the combustion chamber. These conditions correspond to a characteristic gas Reynolds number of $Re_g = 13500$ based on the bluff body diameter, and to a global equivalence ratio of $\phi_g = 0.32$. The flame takes an "M" shape stabilizing over the bluff body in the CRZ. The inner reaction layer interacts with the hollow cone spray, while the outer reaction layer is located in the shearing air flow at the edge of the bluff body. The design of the burner and the carefully selected operating conditions promote unsteady effects, resulting in the intermittent lift-off of the outer reaction

zone. (Cavaliere et al., 2013) Although, the global equivalence ratio of the system is lean, a locally rich region is formed on the bluff body in the CRZ. (Giusti et al., 2016)

METHODOLOGY

The spray flame is simulated using our in-house multi-physics finite element code: Alya. (Vázquez et al., 2016) An Eulerian representation of the turbulent reacting gas phase is coupled with Lagrangian particle transport. These two components are described below, followed by a detailed description of the thermo-chemical tables and the summary of the numerical setup of the different cases. For further details on the numerical formulation, and the application of Alya on turbulent reacting flows see the previous work of the authors. (Both et al., 2020; Mira et al., 2020, 2021; Benajes et al., 2022)

Gas phase modeling

The low Mach number assumption is used to solve the Navier-Stokes equations, i.e.: the hydrodynamic pressure and the gas density are decoupled, thus the gas density is a function of the thermo-chemical state only. Consequently acoustic phenomena are neglected, allowing reasonably large time step size ($\mathscr{O}(1\mu s)$). A non-incremental fractional step method solves the continuity and momentum equations, while a small number of transported scalars describe the gas state: enthalpy, mixture fraction, sub-grid mixture fraction variance, and progress variable. Collocated finite element meshes are used to discretize the simulation domain. Linear finite elements are utilized resulting in a second order discretization in space, while the temporal integration is executed with a third order Runge-Kutta scheme. (Both et al., 2020) The solved partial differential equations are presented below:

$$\partial_t \overline{\rho} + \nabla \cdot (\overline{\rho}\widetilde{\mathbf{u}}) = S^e_\rho, \tag{1}$$

$$\partial_t (\overline{\rho}\widetilde{\mathbf{u}}) + \nabla \cdot (\overline{\rho}\widetilde{\mathbf{u}} \otimes \widetilde{\mathbf{u}}) + \nabla \overline{p} - \nabla \cdot \tau(\widetilde{\mathbf{u}}) = S^e_{\mathbf{u}}, \tag{2}$$

$$\partial_t \left(\overline{\rho}\widetilde{h}\right) + \nabla \cdot \left(\overline{\rho}\widetilde{h}\widetilde{\mathbf{u}}\right) + \nabla \cdot \Phi_h = S^e_h, \tag{3}$$

$$\partial_t \left(\overline{\rho}\widetilde{Z}\right) + \nabla \cdot \left(\overline{\rho}\widetilde{Z}\widetilde{\mathbf{u}}\right) + \nabla \cdot \Phi_Z = S^e_Z, \tag{4}$$

$$\partial_t (\overline{\rho} Z_v) + \nabla \cdot (\overline{\rho} Z_v \widetilde{\mathbf{u}}) + \nabla \cdot \Phi_{Z_v} = -\overline{\rho}\chi^{SGS}_{Z_v} - 2\Phi^{SGS}_Z \cdot \nabla\widetilde{Z} + S^e_{Z_v}, \tag{5}$$

$$\partial_t \left(\overline{\rho}\widetilde{Y}_c\right) + \nabla \cdot \left(\overline{\rho}\widetilde{Y}_c\widetilde{\mathbf{u}}\right) + \nabla \cdot \Phi_{Y_c} = \overline{\dot{\omega}_{Y_c}} + S^e_{Y_c}, \tag{6}$$

where $\overline{\rho}, \widetilde{\mathbf{u}}, \widetilde{h}, \widetilde{Z}, \widetilde{Y}_c$ are the filtered density, velocity, enthalpy, mixture fraction, and progress variable, and Z_v denotes the sub-grid variance of mixture fraction. Non-density weighted LES filtering is marked by a bar and Favre filtering by a tilde as customary.

The total (viscous and sub-grid) stress tensor is: $\tau = (\overline{\mu} + \mu_t)\left(\nabla\widetilde{\mathbf{u}} + \nabla^{\mathrm{T}}\widetilde{\mathbf{u}}\right) - \frac{2}{3}(\overline{\mu} + \mu_t)(\nabla \cdot \widetilde{\mathbf{u}})\mathbf{I}$, which considers the diffusive transport of momentum (Peters, 2001), were $\mathbf{I}$ is the identity tensor, and μ and μ_t are the molecular and sub-grid viscosities respectively. In this work, the sub-grid model of Vreman (2004) is used to evaluate μ_t. The terms: Φ_h, Φ_Z, Φ_{Z_v}, and Φ_{Y_c} denote the total diffusive fluxes of enthalpy, mixture fraction, sub-grid mixture fraction variance, and progress variable respectively. Each scalar flux is composed of a molecular diffusion and a sub-grid scale transport component. For an arbitrary scalar variable $\xi \in \{h, Z, Z_v, Y_c\}$ the total diffusive fluxes are expressed as: $\Phi_\xi = \Phi^D_\xi + \Phi^{SGS}_\xi$, where $\Phi^D_\xi = -\overline{\rho}\widetilde{\mathscr{D}_\xi}\nabla\widetilde{\xi}$ is the flux of molecular diffusion, and $\Phi^{SGS}_\xi = -\frac{\mu_t}{Sc_\xi}\nabla\widetilde{\xi}$ is the flux of sub-grid transport. For the former component the unity Lewis number assumption is followed, i.e. the molecular diffusivity of all the tranported scalars is equal to the thermal diffusivity of the gas mixture: $\widetilde{\mathscr{D}_\xi} = \frac{\overline{\lambda}}{\overline{\rho} c_p}$, where $\overline{\lambda}$ is the filtered thermal conductivity and c_p is the specific heat at the Favre filtered gas composition and enthalpy. Similarly, all the gas phase sub-grid Schmidt numbers are taken equal: $Sc_\xi = 0.7$. The sub-grid variance of mixture fraction is dissipated at the rate of sub-grid scalar dissipation of the resolved mixture fraction, this term is modeled as: $\chi^{SGS}_{Z_v} = 2\frac{Z_v}{\tau_{SGS}}$ where the sub-grid time scale: $\tau_{SGS} = \left(C^2_\varepsilon \frac{\mu_t}{\rho}\frac{|\mathbf{S}|^2}{\Delta^2}\right)^{-1/3}$ is used to characterize the dissipation. The modeling constant: $C_\varepsilon = 3.24$ is a property of the sub-grid model, $\mathbf{S}$ is the strain rate tensor, and Δ is the characteristic filter size equal to the local mesh size in this work. The tabulated chemistry model provides a closure for the material properties and the chemical source term. The global conservation of properties is ensured by coupling the above equations that only describe the gas phase conservation laws to the Lagrangian particle cloud through source terms: S^e_ρ, $S^e_{\mathbf{u}}$, S^e_h, S^e_Z, $S^e_{Z_v}$, $S^e_{Y_c}$, for mass, momentum, enthalpy, mixture fraction, mixture fraction variance, and progress variable respectively. The evaporating mass is the source term of mass conservation, and the same source terms is utilized for the gas phase mixture fraction: $S^e_Z = S^e_\rho$. The spray effect on the sub-grid mixture fraction variance is neglected here: $S^e_{Z_v} = 0$. (Ma and Roekaerts, 2016) Note, however, that if the above equations are converted to the non-conservative form, then dilution terms arise due to the presence of the mass source term.

Liquid phase modeling

The evaporating spray cloud is represented by Lagrangian particles transported in the computational domain. Each numerical particle is characterized by a set of ordinary differential equations (ODE) that capture the evolution of their location, velocity, mass, and temperature. The droplet motion is tracked using a Newmark/Newton-Rhapson time integration scheme developed by Houzeaux et al. (2016), with the drag determined by the correction of Naumann and Schiller (1935). The evaporation model of Abramzon and Sirignano (1989) has been recently found to provide a simple yet adequate closure for heat and mass transfer (Both et al., 2022), thus it is used in this work. The ODEs describing the evolution of individual droplet temperature T_p and droplet mass m_p are:

$$\frac{\mathrm{d}T_p}{\mathrm{d}t} = \frac{\pi d_p \lambda_m N u_m^{*,AS}}{m_p c_{p,p}} (T_s - T_p) \frac{\ln(1+B_T)}{B_T} + \frac{L_v}{m_p c_{p,p}} \frac{\mathrm{d}m_p}{\mathrm{d}t}, \tag{7}$$

$$\frac{\mathrm{d}m_p}{\mathrm{d}t} = -\pi d_p \rho_m \mathscr{D}_m S h_m^{*,AS} \ln(1+B_M), \tag{8}$$

where d_p is the droplet diameter, λ_m the mean gas thermal conductivity, $c_{p,p}$ the droplet specific heat, $Nu_m^{*,AS}$ the corrected Nusselt number, T_s the seen gas temperature, B_T the Spalding heat transfer number, and L_v the latent heat of evaporation. The terms in the mass transfer ODE are: ρ_m the mean gas density, $\mathscr{D}_m$ the mean molecular diffusivity of the fuel vapour in the gas, $Sh_m^{*,AS}$ the corrected Sherwood number, and B_M the Spalding mass transfer number. The droplet interface vapor mass fraction is evaluated assuming local thermodynamic equilibrium. The mean gas properties are taken using the "1/3-law" (Yuen and Chen, 1976) adapted for using the thermo-chemical tables. I.e.: a first order Taylor-expansion of λ, μ and $\mathscr{D}$ is tabulated in terms of temperature, so good approximations can be provided, given the temperature of the "1/3-law". This temperature is used directly in conjunction with the NASA polynomials and the ideal gas law, to obtain the representative specific heat, and the representative density. The exact same approach is used irrespective of the utilized tables. The liquid and phase change properties of the fuels are evaluated as a function of the droplet temperature following Daubert and Danner (1985). The Reynolds number dependence of the uncorrected Nusselt and Sherwood numbers are taken into account using the correlation of Ranz and Marshall (1952).

Tabulated chemistry approaches

The presented tabulated chemistry models map the solutions of 1D flamelets onto a rectilinear table in an *a priori* calculation. These tables are used in the CFD calculation to lookup different properties and provide closure for Eqs. (1)-(8). In all flamelet calculations, the skeletal mechanism of Lu and Law (2006) is utilized, containing 188 species, and 939 reactions. The flamelet inlet conditions are selected based on the operating conditions of the burner. (Both et al., 2021*b*) The four different flamelet sets are illustrated in Fig. 2 by the adiabatic flame temperature (T^b) as function of the equivalence ratio in case of the premixed flamelets, and by the temperature of the stoichiometric mixture (T_{st}) in case of counterflow diffusion flamelets. The premixed flamelets are calculated using the Cantera chemistry library. Decreased enthalpy states are introduced by using a burner-stabilized configuration besides free flamelets, as proposed by Van Oijen and De Goey (2000). The applicability of this heat loss method for spray combustion was subsequently confirmed by Sacomano Filho et al. (2018). Pure fuel and oxidizer are appended to the premixed manifold to cover all possible mixtures. A one dimensional flamelet solver: Chem1D is used for the counterflow diffusion flamelets. (Ramaekers, 2011) In these cases enthalpy loss is introduced by radiation. In all cases, the manifolds are appended with a layer of cold reaction products and reactants, thus they are capable of representing any states down to complete quenching due to heat loss. The non-premixed tabulation methods based on these flamelets may combine stable and unstable flamelets (Stab.+Unstab.) following the Steady Flamelet Progress Variable approach of Pierce and Moin (2004). Chrigui et al. (2012) modified this approach, by replacing the unstable branch with temporal samples taken from an unsteady extinguishing flamelet. (Stab.+Ext.) Finally, the last method assessed here (Reign.+Ext.) is a subset of the Unsteady Flamelet Progress Variable method of Ihme and See (2010), where a single strain rate is selected to compute the reigniting and extinguishing flamelets. Such a simplification is often used in the modeling of autoigniting spray flames. (Mira et al., 2021)

The thermo-chemical states along these flamelets are uniquely characterized by $N_C = 3$ control variables: mixture fraction of Bilger et al. (1990) (Z), progress variable (Y_c), the enthalpy (h). The progress variable is defined as: $Y_c = \frac{4Y_{CO_2}}{W_{CO_2}} + \frac{Y_{CO}}{W_{CO}} + \frac{2Y_{H_2O}}{W_{H_2O}} + \frac{0.5Y_{H_2}}{W_{H_2}}$ following Ma (2016). The progress variable and enthalpy are conditionally scaled, creating the scaled progress variable: $C = \frac{Y_c - Y_c^{min}(Z)}{Y_c^{max}(Z) - Y_c^{min}(Z)}$ and the scaled enthalpy: $i = \frac{h - h^{min}(Z,C)}{h^{max}(Z,C) - h^{min}(Z,C)}$. The flamelet states are mapped onto a rectilinear discretization of the $Z \times C \times i$ hyper-cube, with 101, 101, and 21 points in each dimensions respectively. The mixture fraction discretization is concentrated around the stoichiometric point. (Both et al., 2021*b*) The properties of the database are PDF-integrated with a presumed β-PDF along mixture fraction, thus the final database is parametrized by: $\widetilde{Z}$, Z_v, $\widetilde{Y_c}$, and $\widetilde{h}$.

The principal difference between the thermo-chemical tables is in the distribution of the progress variable source term $\dot{\omega}_{Y_c}$. This property is illustrated in Fig. 3 for the four databases at five different mixture fractions corresponding

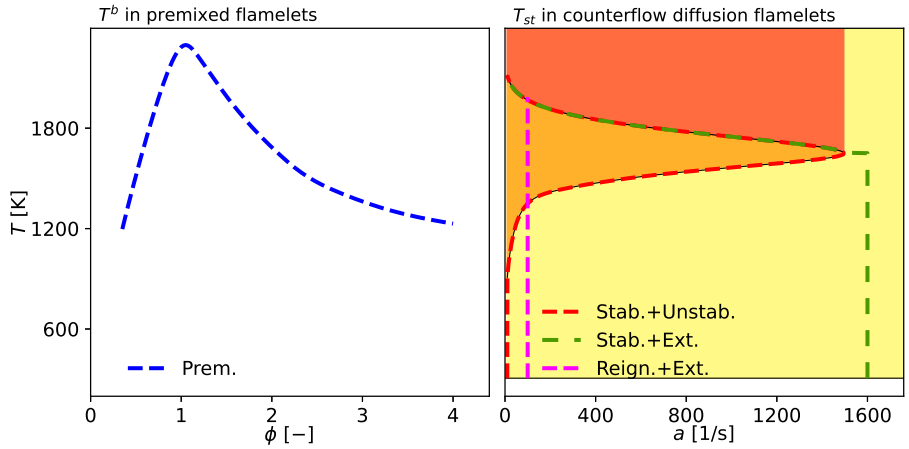

Figure 2 Illustration of applied adiabatic premixed and counterflow diffusion flamelets.

to the equivalence ratios: $\phi \in \{0.3, 0.8, 1.0, 1.5, 3.0\}$. Concentrating first on the counterflow diffusion flames, the figure shows, that the source terms corresponding the unstable branch (Stab.+Unstab.) and to the unsteady extinguishing flamelet (Stab.+Ext.) are fairly close to each other, thus the method of Chrigui et al. (2012) appears to be a justified simplification of the Steady Flamelet Progress Variable model if the evaluation of the unstable branch is infeasible. The extinguishing flamelet produces slightly higher source terms on the lean side. Comparing these two manifolds to the unsteady flamelet reigniting and extinguishing at a constant strain rate of $a = 100/\mathrm{s}$ (Reign.+Ext.), the source terms of this case are consistently lower, especially under very lean ($\phi = 0.3$) and very rich ($\phi = 3.0$) conditions. Finally, the premixed flamelet database (Prem.) can be compared to the counterflow flamelets. As expected, outside the flammability limits, the premixed flamelets predict zero source term, and even at very rich but flammable mixtures ($\phi = 3.0$) the source term is negligible compared to the counterflow diffusion flames. However, at the stoichiometric mixture fraction, and even at $\phi = 0.8$, the premixed flames are the most reactive.

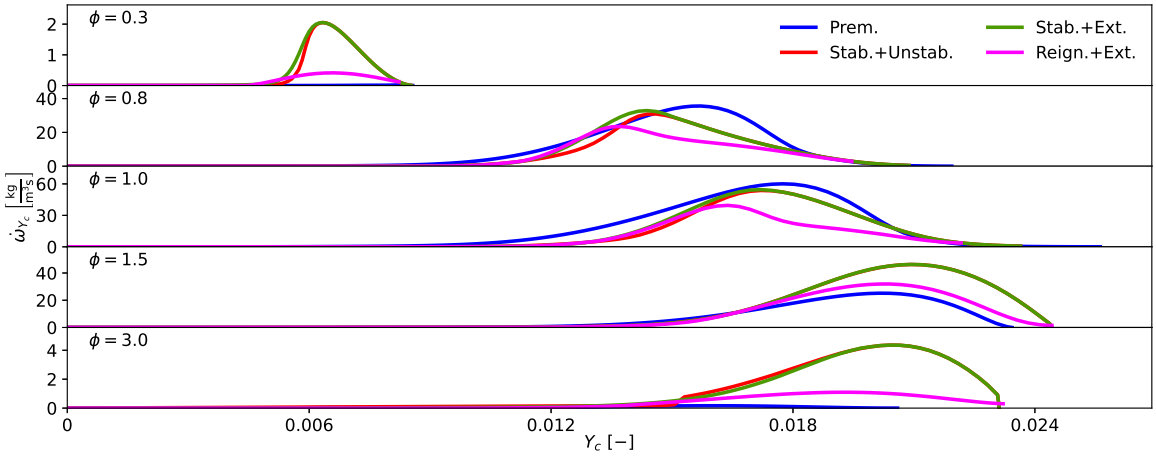

Figure 3 Progress variable source term ($\dot{\omega}_{Y_c}$) along the progress variable (Y_c) in slices of the applied tables at different mixture fractions (identified by the displayed equivalence ratios), the rest of the control variables are kept constant ($i = 1$, $Z_v = 0$).

Numerical setup

The entire air inlet duct with the swirler and the combustion chamber are considered as the computational domain. Two finite element meshes with different element size are used in this work, both composed by hybrid elements with boundary layer refinement in the annular air inlet. Tetrahedral elements are used in the bulk of the flow. A mesh refinement region is concentrated around the bluff body, to capture the intermittent reacting layer. The coarse and fine grids are shown in Fig. 1b and 1c respectively. The coarse grid is characterized by a refinement size of 1 mm in the region of interest yielding a

mesh of 1.2M degrees of freedom, while the element size is half of this in the fine grid: 0.5 mm producing 3.4M degrees of freedom. In both the coarse and fine meshes there is a transition region around the refinement of 2 mm and 1 mm element size respectively, the thickness of this region is increased in the fine mesh as Fig. 1 illustrates. The flame thickness of the premixed flamelets, evaluated based on the maximum temperature gradients, is found to be around $\delta_{th}^{Prem} \approx 0.4$ mm in the highly reactive flamelets near stoichiometry. The same property for highly strained diffusion flamelets is $\delta_{th}^{Diff} \approx 1$ mm. Nevertheless, since a Alya applies a continuous Galerkin method and evaluates the source term integrals with a Gaussian quadrature, it can be argued, that the fine mesh captures the combustion phenomena to an extent. Furthermore, an *a posteriori* analysis of single-point statistics (Mira et al., 2020) of the cases show, that the minimum Kolmogorov scale encountered in the region of interest is: $\eta \approx 0.025$ mm in the annular air inlet. These length scales indicate, that the fine mesh of filter size $\Delta \approx 0.5$ mm is acceptable for LES in terms of resolving the turbulent flow field. However, complete representation of the combustion might require higher resolution.

The flow rate of air is prescribed upstream of the swirler. The air inlet temperature is 288 K, while constant temperature boundary conditions of 700 K are imposed on the vertical and bottom walls of the rectangular combustion chamber and on the flat surface of the bluff body to account for the wall heat loss. The rest of the walls are treated adiabatically. The computational droplets are introduced into the domain at the center of the bluff body, corresponding to the injection location. The initial droplet temperature is the same as the oxidizer: 288 K. The initial droplet size is selected stochastically by a truncated Rosin-Rammler distribution of $\overline{D} = 65$ μm and width parameter $n = 2.5$. The number of injected droplets in each time step is such, that the mean fuel mass flow rate is recovered. Each computational droplet carries the fuel mass corresponding to its volume, thus the concept of "parcels" is not used in this work. The initial droplet velocity is determined to recreate a hollow cone spray pattern. The droplets velocity direction is uniformly distributed azimuthally. The spray half angle is likewise selected randomly in a range cantered at 32° with a span of ±8°. The velocity magnitude is prescribed such, that the axial component of the initial velocity follows a normal distribution with an expected value of 18 m/s and a standard deviation of 10%.

RESULTS AND DISCUSSION

The LES simulations were executed using the 4 different thermo-chemical databases using the 2 computational meshes presented in Fig. 1. The flame stabilization and the location of the hollow cone spray cloud is illustrated on Fig. 4. The flame is anchored on the bluff body, where rich partially reacted gasses are accumulated. The limit of this rich region is situated in the shear-layer at the edge of the bluff body as it is marked by the stoichiometric isosurface. The temperature of this isosurface indicates the presence of localized extinction, that is also captured by the absence of the *OH* radical. As detailed below, only the simulation using the premixed database shows significant lift-off, such as in the time instance illustrated by Fig. 4. The resulting edge flame seldom touches the bluff body, and its location fluctuates as new extinct regions are created by the high shear rate, and as the large scale flow structures disturb the edge flame.

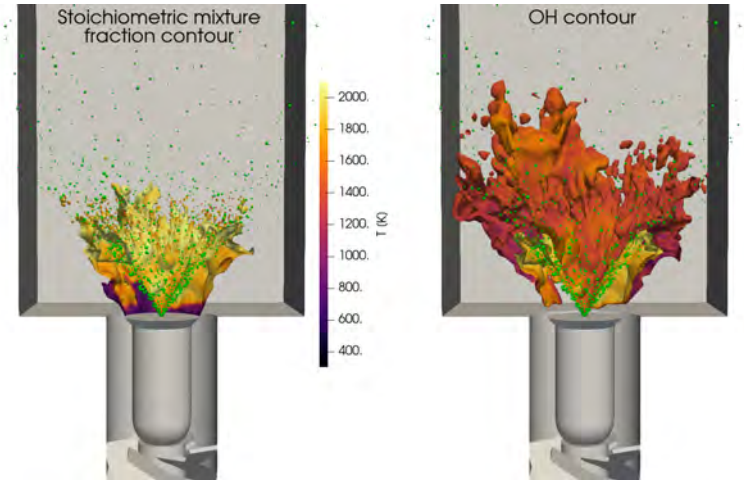

Figure 4 Illustration of the instantaneous LES results on the fine mesh using the premixed flamelet database. Left: isosurface of stoichiometric mixture fraction ($Z_{st} = 0.0622$), right: isosurface of hydroxyl radical mass fraction ($Y_{OH} = 0.0004$), both isosurfaces are colored by the gas phase temperature.

Validation

The results of the 8 different LES simulations are compared to the point-measurement data of Sidey et al. (2017) in Fig. 5. The velocity and size distribution of the droplet cloud is particularly insensitive both to the mesh size and to the

tabulation strategy. For all cases, the core of the spray is well reproduced, with a minor over-prediction of the RMS of the axial velocity. The edge of the hollow cone spray is more challenging to predict, as only few droplets enter into this region, here we observe an under-prediction of the mean velocity and the droplet diameter. Overall, the spray is represented adequately by the Lagrangian particle cloud, as the most important features are correctly reproduced.

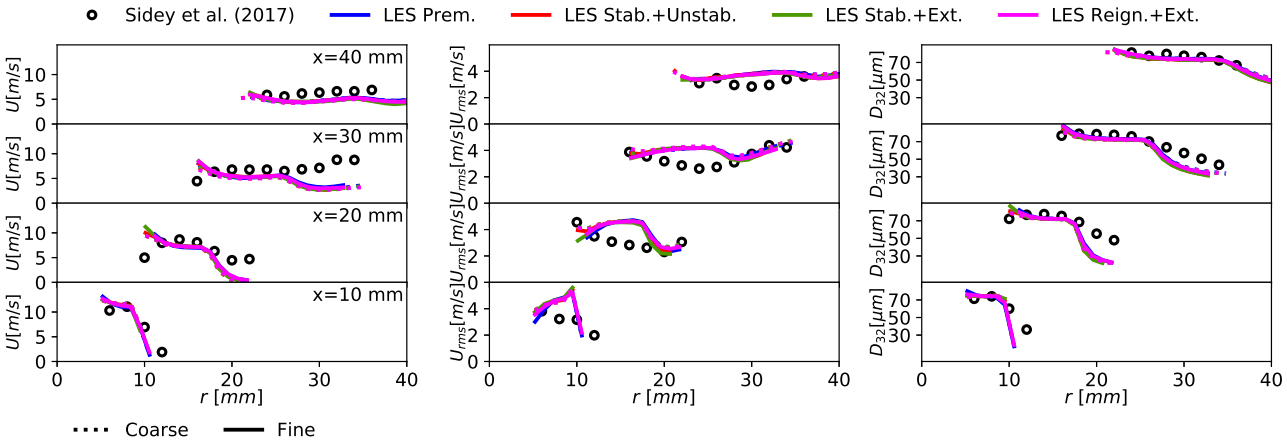

Figure 5 Comparison of the droplet cloud statistics extracted from the LES simulations with the phase Doppler anemometry data of Sidey et al. (2017). Left: mean axial droplet velocity, middle: RMS of axial droplet velocity, right: Sauter mean diameter.

Mean flame behavior

The gas phase fields presented in Fig. 6 are also rather similar using the different manifold representations, however, some differences can be distinguished. In general, the mean axial velocity shows the swirling flow entering the combustion chamber, and impinging on the chamber walls at $x = 40$ mm. The central recirculation zone is characterized by a slight negative mean axial velocity at all axial locations. The momentum exchange between the spray and the flow field is notable, as the secondary mean velocity peak indicates at $x = 10$ mm and $r = 10$ mm. The slight differences in the velocity profiles can be attributed to the mesh, rather than the tabulation strategies, as the coarse mesh size is approximately 40 times larger than the Kolmogorov scale, while the fine mesh is characterized by a more appropriate ratio of 20.

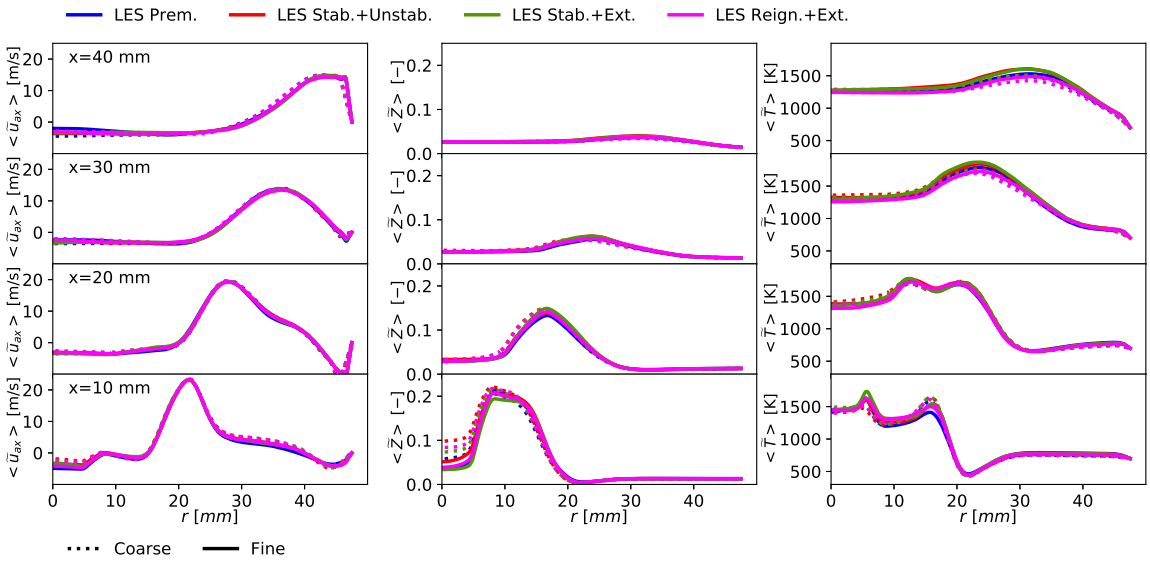

Figure 6 Temporal average of gas-phase fields of the LES simulations. Left: mean axial velocity, middle: mean mixture fraction, right: mean temperature.

The mean mixture fraction field follows closely the spray pattern. More precisely, the peak of the mixture fraction is

generally located at a higher radius than the location of the spray. For example, at $x = 20$ mm the spray is centered around $r = 15$ mm, while the mixture fraction peak is near $r = 19$ mm. This behavior is created by the negative axial velocities of the central recirculation zone, as the freshly evaporated fuel from the spray is carried towards the bluff body by the recirculation. As Fig. 4 also illustrates, the evaporation of the spray creates a conical region of rich mixture, with leaner compositions both in the recirculation zone, and in the fresh oxidizer stream. Note, that possibly due to the higher bulk air velocity and likewise higher initial droplet velocity, this mixture fraction field is significantly leaner, than that reported by Paulhiac et al. (2020). The reacting layers are situated between these lean and rich regions. The mixture fraction shows certain sensitivity to the mesh at $x = 10$ mm near the center of the domain. This region is particularly close to the spray cloud on all sides, thus the fine mesh is needed to correctly capture the evaporative mixture fraction source term, and the behavior of the inner reaction zone.

Finally, Fig. 6 also presents the mean temperature field. Up to $x = 20$ mm the two reacting layers can be clearly distinguished by the temperature peaks, while more downstream there is only one single temperature maximum as the two reacting layers merge. The mesh refinement has a clear effect on the temperature profiles, especially at $x = 10$ mm. The inner reaction zone shows lower temperatures on the coarse mesh, due to the overall higher mixture fractions in the central recirculation zone and the consequent absence of stoichiometric mixture. Meanwhile, the outer reacting layer has a higher mean temperature using the coarse mesh, as refinement results in thinner and more intermittent reaction layers, even if lift-off is not encountered frequently at $x = 10$ mm. The lowest mean temperature at this location is produced by the premixed flamelet tabulation, since this modelling strategy results in the most intermittent flame. Indeed, according to the results of Fig. 7b, the flame edge is lifted above $x = 10$ mm in 14% the studied time instances.

Analysis of flame lift-off

The lift-off statistics are extracted from the OH planar laser induced fluorescence data from the Cambridge Swirl Flames Data Repository (Sidey et al., 2017). The simulation results are processed in a similar manner, using the mass fraction of OH retrieved from the thermo-chemical databases. The lift-off length of the outer reaction layers is measured at different locations as illustrated in Fig. 7a, and the frequency of these lengths falling into 2 mm wide bins centered around the locations shown in Fig. 7b is counted. In general, all presented tabulated chemistry methods predict a higher probability of full attachment than the measured value. As the mesh is refined, the tabulation strategies based on counterflow diffusion flamelets tend to predict an even lower probability of lift-off, while the prediction of the premixed flamelet table is improved. This significant change in the lift-off statistics is an additional confirmation, that the flamelet structures need to be resolved in more detail. On the fine mesh, all the diffusion flamelet tables predict, that the most likely lift-off state is complete attachment. Only the premixed flamelet table results in a lift-off PDF, that is has a mode different from $LOL = 0$ mm.

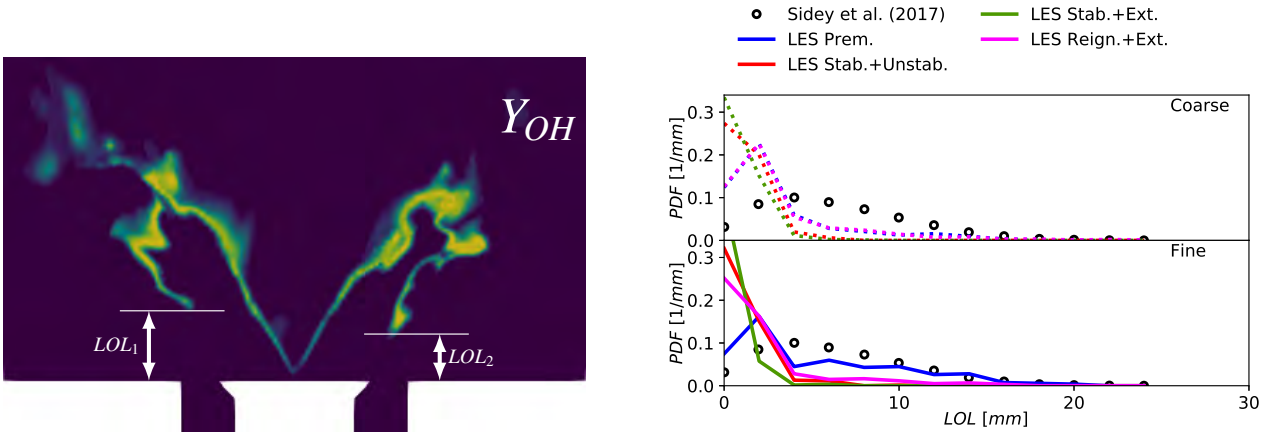

(a) Illustration of the lift-off length definition. **(b) Probability density function of lift-off length.**

Figure 7 Presence of localized extinction with different tabulation strategies.

CONCLUSIONS

Different chemistry tabulation strategies are applied for the LES simulation of the H1S1 n-heptane case of the Cambridge Swirl Spray Flames, including the strategy of Sacomano Filho et al. (2018) using free and burner-stabilized premixed flamelets, and three different strategies involving diffusion flamelets extended to non-adiabatic manifolds. These practically correspond to the models of Pierce and Moin (2004), Chrigui et al. (2012), and Ihme and See (2010). The results are relatively insensitive to the choice of the table, in terms of time averaged quantities as the flame stabilization is hydrodynamically driven in this configuration. However, significant differences are observed in the finite-rate effects displayed

by the flame, that are quantified through the lift-off length statistics. Namely, the tabulation strategy based on premixed flamelets provides the best lift-off prediction. As emphasized by many recent studies on the topic of tabulated chemistry methods for partially-premixed combustion, this result is not trivial. On one hand, this highlights the need to adapt more sophisticated tabulated chemistry methods to turbulent combustion such as the one proposed by Franzelli et al. (2013) or Illana et al. (2021), and incorporate them into the best practices of the aerospace industry. On the other hand, more work is needed to identify the cases where classical models are indeed sufficient, especially in relation to the expected mixture fraction stratification.

ACKNOWLEDGMENTS

The research leading to these results has received funding from the European Union's Horizon 2020 Programme under the CoEC project, grant agreement No. 952181 and the Clean Sky 2 Joint Undertaking ESTiMatE project under grant agreement No 821418.

References

Abramzon, B. and Sirignano, W. A. (1989), 'Droplet vaporization model for spray combustion calculations', *International journal of heat and mass transfer* **32**(9), 1605–1618.

Benajes, J., García-Oliver, J. M., Pastor, J. M., Olmeda, I., Both, A. and Mira, D. (2022), 'Analysis of local extinction of a n-heptane spray flame using large-eddy simulation with tabulated chemistry', *Combustion and Flame* **235**, 111730.

Bilger, R., Stårner, S. and Kee, R. (1990), 'On reduced mechanisms for methane/air combustion in nonpremixed flames', *Combustion and Flame* **80**(2), 135–149.

Both, A., Lehmkuhl, O., Mira, D. and Ortega, M. (2020), 'Low-dissipation finite element strategy for low Mach number reacting flows', *Computers & Fluids* **200**, 104436.

Both, A., Mira, D. and Lehmkuhl, O. (2021*a*), LES study of the impact of fuel composition on a swirl spray flame approaching blow-off, *in* '13th International ERCOFTAC Symposium on Engineering Turbulence Modelling and Measurements', pp. 527–532.

Both, A., Mira, D. and Lehmkuhl, O. (2021*b*), Optimization of the progress variable definition using a genetic algorithm for the combustion of complex fuels, *in* '10th European Combustion Meeting: April 14-15, 2021, virtual edition: proceedings volume', MCM, pp. 1145–1151.

Both, A., Mira, D. and Lehmkuhl, O. (2022), 'Evaporation of volatile droplets subjected to flame-like conditions', *International Journal of Heat and Mass Transfer* **187**, 122521.

Cavaliere, D. E., Kariuki, J. and Mastorakos, E. (2013), 'A comparison of the blow-off behaviour of swirl-stabilized premixed, non-premixed and spray flames', *Flow, turbulence and combustion* **91**(2), 347–372.

Chrigui, M., Gounder, J., Sadiki, A., Masri, A. R. and Janicka, J. (2012), 'Partially premixed reacting acetone spray using les and fgm tabulated chemistry', *Combustion and flame* **159**(8), 2718–2741.

Daubert, T. E. and Danner, R. P. (1985), *Data compilation tables of properties of pure compounds*, Design Institute for Physical Property Data, American Institute of Chemical Engineers.

Elasrag, H. and Li, S. (2018), Investigation of extinction and reignition events using the flamelet generated manifold model, *in* 'Turbo Expo: Power for Land, Sea, and Air', Vol. 51050, American Society of Mechanical Engineers, p. V04AT04A023.

Fiorina, B., Veynante, D. and Candel, S. (2015), 'Modeling combustion chemistry in large eddy simulation of turbulent flames', *Flow, Turbulence and Combustion* **94**(1), 3–42.

Foale, J. M., Giusti, A. and Mastorakos, E. (2021), Simulating the blowoff transient of a swirling, bluff body-stabilized kerosene spray flame using detailed chemistry, *in* 'AIAA Scitech 2021 Forum', p. 0187.

Franzelli, B., Fiorina, B. and Darabiha, N. (2013), 'A tabulated chemistry method for spray combustion', *Proceedings of the Combustion Institute* **34**(1), 1659–1666.

Franzelli, B., Vié, A., Boileau, M., Fiorina, B. and Darabiha, N. (2017), 'Large eddy simulation of swirled spray flame using detailed and tabulated chemical descriptions', *Flow, Turbulence and Combustion* **98**(2), 633–661.

Giusti, A., Kotzagianni, M. and Mastorakos, E. (2016), 'Les/cmc simulations of swirl-stabilised ethanol spray flames approaching blow-off', *Flow, Turbulence and Combustion* **97**(4), 1165–1184.

Giusti, A. and Mastorakos, E. (2017), 'Detailed chemistry LES/CMC simulation of a swirling ethanol spray flame approaching blow-off', *Proceedings of the Combustion Institute* **36**(2), 2625–2632.

Houzeaux, G., Garcia, M., Cajas, J. C., Artigues, A., Olivares, E., Labarta, J. and Vázquez, M. (2016), 'Dynamic load balance applied to particle transport in fluids', *International Journal of Computational Fluid Dynamics* **30**(6), 408–418.

Ihme, M. and See, Y. C. (2010), 'Prediction of autoignition in a lifted methane/air flame using an unsteady flamelet/progress variable model', *Combustion and Flame* **157**(10), 1850–1862.

Illana, E., Mira, D. and Mura, A. (2021), 'An extended flame index partitioning for partially premixed combustion', *Combustion Theory and Modelling* **25**(1), 121–157.

Lu, T. and Law, C. K. (2006), 'Linear time reduction of large kinetic mechanisms with directed relation graph: n-heptane and iso-octane', *Combustion and Flame* **144**(1), 24–36.

Ma, L. (2016), Computational modeling of turbulent spray combustion, PhD thesis, Delft University of Technology.

Ma, L. and Roekaerts, D. (2016), 'Modeling of spray jet flame under mild condition with non-adiabatic fgm and a new conditional droplet injection model', *Combustion and Flame* **165**, 402–423.

Mira, D., Lehmkuhl, O., Both, A., Stathopoulos, P., Tanneberger, T., Reichel, T. G., Paschereit, C. O., Vázquez, M. and Houzeaux, G. (2020), 'Numerical characterization of a premixed hydrogen flame under conditions close to flashback', *Flow, Turbulence and Combustion* **104**(2), 479–507.

Mira, D., Pérez-Sánchez, E. J., Surapaneni, A., Benajes, J., García-Oliver, J. M., Pastor, J. M. and De León, D. (2021), Les study on spray combustion with renewable fuels under ecn spray-a conditions, *in* 'Internal Combustion Engine Division Fall Technical Conference', Vol. 85512, American Society of Mechanical Engineers, p. V001T06A004.

Naumann, Z. and Schiller, L. (1935), 'A drag coefficient correlation', *Zeitschrift Verein Deutscher Ingenieure* **77**, 318–323.

Olguin, H. and Gutheil, E. (2014), 'Influence of evaporation on spray flamelet structures', *Combustion and Flame* **161**(4), 987–996.

Paulhiac, D., Cuenot, B., Riber, E., Esclapez, L. and Richard, S. (2020), 'Analysis of the spray flame structure in a lab-scale burner using large eddy simulation and discrete particle simulation', *Combustion and Flame* **212**, 25–38.

Peters, N. (2001), *Turbulent combustion*, IOP Publishing.

Pierce, C. D. and Moin, P. (2004), 'Progress-variable approach for large-eddy simulation of non-premixed turbulent combustion', *Journal of fluid Mechanics* **504**, 73–97.

Pitsch, H. (2006), 'Large-eddy simulation of turbulent combustion', *Annu. Rev. Fluid Mech.* **38**, 453–482.

Ramaekers, W. (2011), 'Development of flamelet generated manifolds for partially-premixed flame simulations'.

Ranz, W. E. and Marshall, W. R. (1952), 'Evaporation from drops: Part 1', *Chem. eng. prog* **48**(3), 141–146.

Sacomano Filho, F. L., Speelman, N., van Oijen, J. A., de Goey, L. P. H., Sadiki, A. and Janicka, J. (2018), 'Numerical analyses of laminar flames propagating in droplet mists using detailed and tabulated chemistry', *Combustion Theory and Modelling* **22**(5), 998–1032.

Sidey, J. A. M., Giusti, A., Benie, P. and Mastorakos, E. (2017), 'The swirl flames data repository'.
URL: *http://swirlflame.eng.cam.ac.uk*

Van Oijen, J. and De Goey, L. (2000), 'Modelling of premixed laminar flames using flamelet-generated manifolds', *Combustion science and technology* **161**(1), 113–137.

Van Oijen, J. and De Goey, L. (2004), 'A numerical study of confined triple flames using a flamelet-generated manifold', *Combustion Theory and Modelling* **8**(1), 141.

Vázquez, M., Houzeaux, G., Koric, S., Artigues, A., Aguado-Sierra, J., Arís, R., Mira, D., Calmet, H., Cucchietti, F., Owen, H. et al. (2016), 'Alya: Multiphysics engineering simulation toward exascale', *Journal of computational science* **14**, 15–27.

Vreman, A. (2004), 'An eddy-viscosity subgrid-scale model for turbulent shear flow: Algebraic theory and applications', *Physics of fluids* **16**(10), 3670–3681.

Yuen, M. C. and Chen, L. W. (1976), 'On drag of evaporating liquid droplets', *Combustion Science and Technology* **14**(4-6), 147–154.